



Effect of viscosity on harmonic signals from magnetic fluid



Takashi Yoshida*, Shi Bai, Aiki Hirokawa, Kazuhiro Tanabe, Keiji Enpuku

Department of Electrical and Electronic Engineering, Kyushu University, Fukuoka 819-0395, Japan

ARTICLE INFO

Article history:

Received 20 June 2014

Received in revised form

9 October 2014

Accepted 9 October 2014

Available online 18 October 2014

Keywords:

Magnetic fluid

Magnetic particle imaging

Brownian relaxation

Néel relaxation

Stochastic LLG equation

Langevin equation

ABSTRACT

We explored the effect of viscosity on harmonic signals from a magnetic fluid. Using a numerical simulation that accounts for both the Brownian and Néel processes, we clarified how the magnetization mechanism is affected by viscosity. When the excitation field varies much slower than the Brownian relaxation time, magnetization can be described by the Langevin function. On the other hand, for the case when the excitation field varies much faster than the Brownian relaxation time, but much slower than the Néel relaxation time, the easy axes of the magnetic nanoparticles (MNPs) turn to some extent toward the direction of the excitation field in an equilibrium state. This alignment of the easy axes of MNPs caused by the AC field becomes more significant with the increase of the AC field strength. Consequently, the magnetization is different from the Langevin function even though Néel relaxation time is faster than time period of the external frequency. It is necessary to consider these results when we use harmonic signals from a magnetic fluid in a high-viscosity medium.

© 2014 Elsevier B.V. All rights reserved.

1. Introduction

Magnetic nanoparticles (MNPs) in solution, i.e., magnetic fluids, have been widely studied for biomedical applications such as separation of biological targets, immunoassays, drug delivery, hyperthermia, and magnetic particle imaging (MPI) [1]. MPI presents a new modality for imaging the spatial distribution of MNPs, especially for in-vivo diagnostics [2]. Thus far, several methods, such as harmonic-space MPI [2–4], narrowband MPI, [5] and x-space MPI [6,7], have been introduced to reconstruct the image of the spatial distribution of the MNPs in MPI. In harmonic-space MPI, harmonic signals generated by the nonlinear magnetization of MNPs exposed to both an AC excitation field and a DC gradient field are detected to image the spatial distribution of MNPs.

In order to characterize or optimize the MNPs for MPI application, harmonic magnetization signals from MNPs have been studied. In Ref. [8], the Langevin function, which describes the static magnetization of superparamagnetic MNPs, was used to evaluate the harmonic signals. In order to take the finite relaxation time into account, a modified Langevin function was used in Refs. [9,10]. However, this modified Langevin function has not been theoretically established. On the other hand, in Ref. [11], the stochastic Landau–Lifshitz–Gilbert (LLG) equation, which takes into account thermal fluctuations, was used to evaluate the harmonic signals from MNPs for MPI application. While the stochastic LLG

equation describes the dynamic behavior of the magnetization of MNPs, the numerical simulation in Ref. [11] was restricted to the case of immobilized MNPs.

It is well recognized that magnetization in a magnetic fluid occurs via Néel and Brownian processes. Since the Brownian relaxation time is proportional to the viscosity of the surrounding medium and the viscosity may change in practical applications, it is important to investigate the effect of viscosity on the harmonic signals from a magnetic fluid.

In this study, we investigate the dynamic behavior of MNPs by considering both the Néel and Brownian relaxations. We first show that the measured third harmonic signals from two magnetic fluid samples with different viscosities exhibit different properties. Then, the effect of viscosity on the mechanism of magnetization in the magnetic fluid is clarified with a numerical simulation. Finally, based on the numerical simulation results, we obtain some empirical equations for the magnetization of MNPs.

2. Experimental

2.1. Materials and methods

In the experiment, commercial MNPs called Resovist (FUJIFILM RI Pharma) were used as samples. Resovist is a hydrophilic colloidal solution of $\text{Fe}_3\text{O}_4/\gamma\text{Fe}_2\text{O}_3$ nanoparticles coated with carboxydextran, which has a primary core diameter in the range of 5–10 nm. It consists of clusters of elementary particles. The iron

* Corresponding author.

E-mail address: t_yoshi@ees.kyushu-u.ac.jp (T. Yoshida).

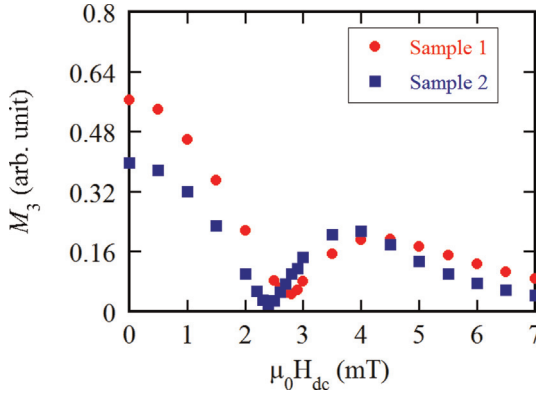


Fig. 1. Experimental results of the third harmonics vs. DC field when an excitation field with $\mu_0 H_{ac}=3$ mT and $f=1$ kHz was applied. Samples 1 and 2 were diluted with pure water and glycerol, respectively.

concentration of the original Resovist magnetic fluid is 27.875 mg (Fe)/ml.

To investigate the effect of viscosity on harmonic signals from a magnetic fluid, we prepared two samples. In sample 1, 60 μ l of the Resovist magnetic fluid was diluted in 230 μ l of pure water, while in sample 2, 230 μ l of glycerol was substituted in place of water. These two samples differ in viscosity.

In the experiment, an external field, $H=H_{dc}+\sqrt{2}H_{ac}\sin(2\pi ft)$, was applied via an excitation coil. The magnetic signal from the MNPs was detected using an inductive pickup-coil gradiometer installed concentrically with the excitation coil. In order to avoid interference from the excitation field, a first-order gradiometer was used.

2.2. Experimental results

In Fig. 1, experimental results of the third harmonic signal vs. DC field are shown. AC excitation field with $\mu_0 H_{ac}=3$ mT and $f=1$ kHz was applied. As shown, the DC field dependence of the third harmonic was different between the two samples, which indicated that viscosity affected the third harmonic signal. Since the DC field dependence of the harmonic signal is directly related to the spatial resolution in MPI, this result implies that spatial resolution is also affected by the viscosity of the magnetic fluid.

We note that the vertical axis, M_3 , represents the absolute value of the third harmonic signal. It can be shown from the Langevin function that the third harmonic signal decreases, becomes zero at a certain DC field, and then becomes negative values when the DC field is increased [12]. Therefore, if we plot the absolute value of the third harmonic signal, it shows the sharp minimum at a certain DC field, as shown in Fig. 1.

3. Numerical simulation

3.1. Methods

We performed numerical simulations to study the mechanism causing the difference in third harmonics between samples 1 and 2. When the MNPs can rotate physically, the dynamics of the magnetic moment is determined by a combination of Brownian and Néel processes.

The dynamics of a unit vector along the easy axis \vec{n} is given by the Langevin equation [13]

$$\frac{d\vec{n}}{dt} = \frac{1}{\eta\pi d_h^3} \vec{m} \times \vec{B} \times \vec{n} + \sqrt{\frac{k_B T}{\eta\pi d_h^3}} \vec{\Gamma} \times \vec{n}, \quad (1)$$

where η is the viscosity of the surrounding medium, d_h is the hydrodynamic size of the MNP, \vec{m} is the magnetic moment vector of the MNP, and $k_B T$ is the thermal energy. The random torque, $\vec{\Gamma}$, on the MNP caused by thermal fluctuations satisfies the following equations:

$$\langle \vec{\Gamma}_i \rangle = 0, \quad (2)$$

$$\langle \vec{\Gamma}_i(t) \vec{\Gamma}_j(t') \rangle = 2\delta_{ij}\delta(t-t'). \quad (3)$$

Here, $\langle \rangle$ represents the average over an ensemble, i and j are Cartesian indices, δ_{ij} is the Kronecker delta function, and δ is the Dirac delta function.

On the other hand, the dynamics of the magnetic moment vector \vec{m} is given by [13]

$$\frac{d\vec{m}}{dt} = \gamma \vec{m} \times (\vec{B}_{eff} + \vec{B}_{th}) - \gamma \frac{\lambda}{m} \vec{m} \times [\vec{m} \times (\vec{B}_{eff} + \vec{B}_{th})] \quad (4)$$

where γ is the gyromagnetic ratio and λ is a dimensionless damping coefficient. \vec{B}_{eff} is the effective magnetic field given by

$$\vec{B}_{eff} = \vec{B}_{ex} + \vec{B}_{ani}, \quad (5)$$

$$\vec{B}_{ani} = \frac{2KV_c}{m} \frac{\vec{m} \cdot \vec{n}}{m} \vec{n}, \quad (6)$$

where \vec{B}_{ex} is the external field and \vec{B}_{ani} is the magnetic-anisotropy field. \vec{B}_{th} , the fluctuating magnetic field due to thermal noise, satisfies the following equations:

$$\langle \vec{B}_{th,i}(t) \rangle = 0, \quad (7)$$

$$\langle \vec{B}_{th,i}(t) \vec{B}_{th,j}(t') \rangle = \frac{2\lambda}{1+\lambda^2} \frac{k_B T}{\gamma m} \delta_{ij} \delta(t-t') \quad (8)$$

Eq. (4) is a stochastic LLG equation in which thermal fluctuations are taken into account.

The dynamic behavior of the magnetic moment as well as the easy axis for a single MNP can be calculated by solving Eqs. (1) and (4) simultaneously. In the simulation, Eqs. (1) and (4) were discretized with respect to time t . The discretization interval Δt was set to $0.01\tau_{N0}$, and the value $\lambda=0.1$ was used. Here, $\tau_{N0}=m/(2\gamma\lambda E_B)=10^{-9}$ is the characteristic Néel relaxation time, $E_B=K\pi d_c^3/6$ is the anisotropy energy barrier, K is the anisotropy constant, and d_c is the core size of the MNP. The dynamics of the magnetic moment vector \vec{m} and unit vector along the easy axis \vec{n} were calculated for $N=7168$ MNPs. Consequently, the average value $\langle \vec{m} \rangle$ over the ensemble was obtained. The numerical simulation was carried out until an equilibrium magnetization was obtained. The harmonic spectrum of the magnetization was obtained by performing a Fourier transform on this equilibrium magnetization.

For simplicity, we assumed that all the MNPs have the same values of m and E_B in the simulation, although the real Resovist sample has a size distribution. In Ref. [11], it was shown that Resovist MNPs with $15\text{ nm} < d_c < 40\text{ nm}$ size distribution exhibited a rich harmonic spectrum. Therefore, we set $d_c=28\text{ nm}$ in the simulation. Further, $M_s=360\text{ kA/m}$, $K=4\text{ kJ/m}^3$, and $t_{co}=7\text{ nm}$ were used, as described in Ref. [11]. Here, $t_{co}=(d_h-d_c)/2$ is the thickness of the coating material. The Néel relaxation time was calculated to

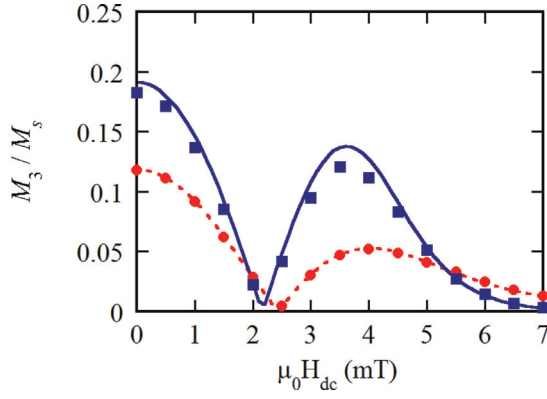


Fig. 2. Numerical simulation results of the third harmonics vs. DC field when an excitation field with $\mu_0 H_{ac} = 3$ mT and $f = 1$ kHz was applied. Circles and squares show the numerical simulation results with stochastic Eqs. (1) and (4) for samples 1 and 2, respectively. The dotted line is calculated with the Langevin function. The solid line is calculated using Eqs. (15)–(18).

be $\tau_N = \tau_{N0} \exp(E_B/k_B T) = 6.7 \times 10^{-5}$ s at $T = 300$ K, and the magnetic moment was calculated to be $m = M_s \pi d_c^3 / 6 = 4.14 \times 10^{-18}$ A m². Assuming that the values of viscosities of sample 1 diluted with pure water and sample 2 diluted with glycerol are 1 mPa s and 100 mPa s, respectively, Brownian relaxation times were calculated to be $\tau_B = \eta d_h^3 / 2 k_B T = 2.8 \times 10^{-5}$ s for sample 1 and

$\tau_B = 2.8 \times 10^{-3}$ s for sample 2. We confirmed that these Brownian relaxation times used in the numerical simulation are reasonable by measuring the frequency dependences of the AC susceptibilities of samples 1 and 2.

3.2. Simulation results

3.2.1. DC field dependence of the harmonic signal

In Fig. 2, we show simulation results of the DC field dependence of the harmonic signal obtained for samples 1 (circles) and 2 (squares) when an AC field of $\mu_0 H_{ac} = 3$ mT is applied. The dotted line was calculated using a Langevin function with $m = 4.14 \times 10^{-18}$ A m². The simulation result for sample 1 (circles) agreed well with the Langevin function. On the other hand, the simulation result for sample 2 (squares) was very different from that expected from the Langevin function. The third harmonic signal decreased with increasing DC field more rapidly than the Langevin function. We note that such strong field dependence was observed in the experiment, as shown in Fig. 1.

3.2.2. Behaviors of the easy axes

In order to study the effect of viscosity in more detail, we first discuss the behaviors of the easy axes of MNPs when an AC field is applied. In Fig. 3(a), simulation results of the behaviors of the easy axes in an equilibrium state are shown for $H_{dc} = 0$ and $\mu_0 H_{ac} = 3$ mT with $f = 1$ kHz. Here, we define $\theta_{ea,i}$ as the angle between the

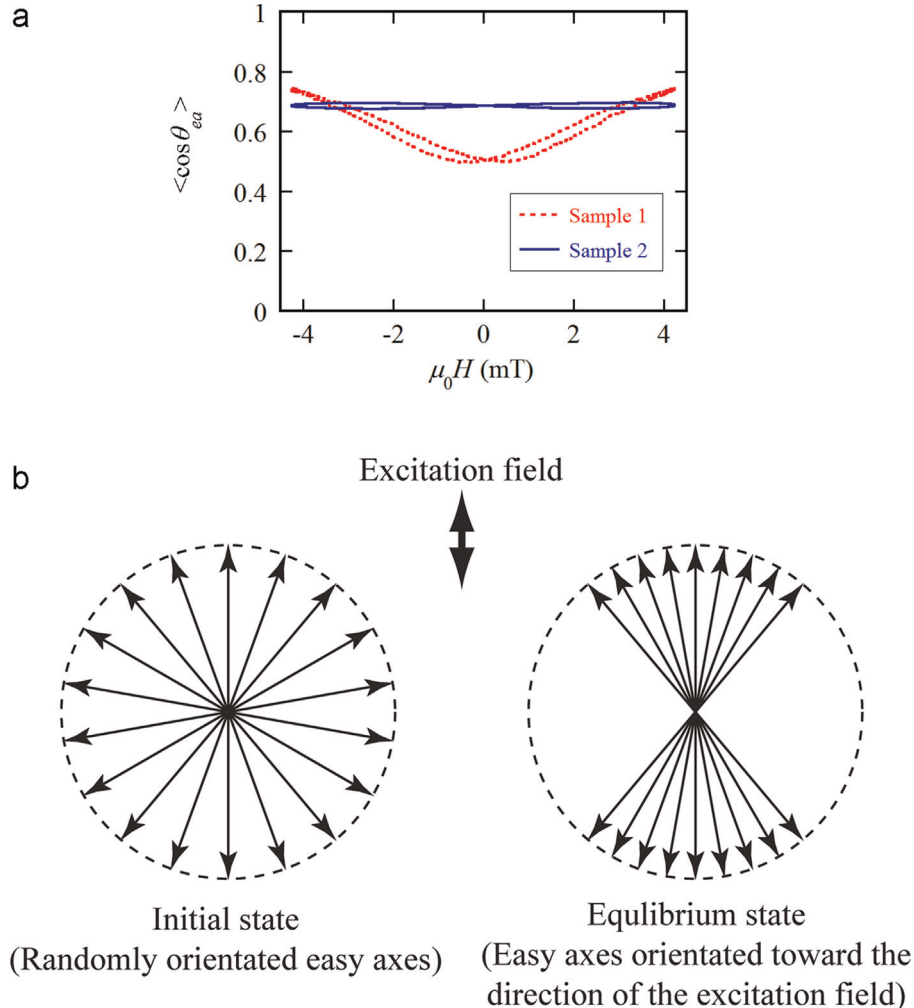


Fig. 3. (a) Simulation results of the behaviors of the easy axes of samples 1 and 2 in an equilibrium state when $H_{dc} = 0$ and $\mu_0 H_{ac} = 3$ mT with $f = 1$ kHz. (b) Schematic of the distribution of easy axes of sample 2 when the AC field is applied.

direction of the easy axis \vec{n} of the i th particle and the external field \vec{H} . The value of $\langle \cos \theta_{ea} \rangle$, which is an ensemble average over N particles, is calculated as

$$\langle \cos \theta_{ea} \rangle(t) = \frac{1}{N} \sum_{i=1}^N \cos \theta_{ea,i}(t). \quad (9)$$

Fig. 3(a) represents the trace of $\langle \cos \theta_{ea} \rangle$ as a function of $\mu_0 H(t) = \mu_0 \sqrt{2} H_{ac} \sin(2\pi f t)$. As can be seen, for sample 1, $\langle \cos \theta_{ea} \rangle$ changes with respect to the external field $H(t)$. This indicates that the ensemble average of the angle of the easy axis rotates with the external field $H(t)$. We note that this rotation is caused by the Brownian rotation of MNPs. Since τ_B for sample 1 is smaller than the inverse of the excitation frequency, f , it is natural that magnetization occurs via the Brownian process.

On the other hand, for sample 2, $\langle \cos \theta_{ea} \rangle$ is almost constant, as shown in Fig. 3(a). This indicates that the ensemble average of the angle of the easy axis does not rotate with the external field $H(t)$ in an equilibrium state. This is because the Brownian rotation of MNPs is prohibited: τ_B of sample 2 is much larger than the inverse of the excitation frequency, f . In this case, magnetization occurs via the Néel process because $\tau_N < 1/2\pi f$.

However, it should be noted that the easy axes for sample 2 are not randomly orientated. We note that $\langle \cos \theta_{ea} \rangle = 0.5$ when the easy axes are randomly orientated. However, for sample 2, $\langle \cos \theta_{ea} \rangle$ is around 0.69, as shown in Fig. 3(a). This indicates that easy axes are orientated toward the direction of the excitation field.

Fig. 3(b) shows the schematic of the distribution of easy axes of sample 2 when the AC field is applied. Before applying the AC field, i.e., in the initial state, the easy axes are randomly orientated. On applying the AC field, the easy axes turn to some extent toward the direction of the excitation field in an equilibrium state, as schematically shown in Fig. 3(b). Mamiya et al. first reported this interesting phenomenon [14]. In short, for the case $\tau_N \ll 1/2\pi f \ll \tau_B$, the AC field gradually rotates the easy axes towards the direction of the excitation field.

We investigated how the value of $\langle \cos \theta_{ea} \rangle$ of sample 2 depends on the strength of the external field. Fig. 4(a) represents the traces of $\langle \cos \theta_{ea} \rangle$ when H_{ac} changed from $\mu_0 H_{ac} = 1$ –5 mT with $H_{dc} = 0$. Fig. 4(b) shows the dependence of $\langle \cos \theta_{ea} \rangle$ on H_{ac} . As shown, $\langle \cos \theta_{ea} \rangle$ is around 0.5 when $\mu_0 H_{ac} = 1$ mT, indicating that the easy axes are randomly orientated in this case. When H_{ac} was increased, the value of $\langle \cos \theta_{ea} \rangle$ increased to 0.8, indicating that orientation of the easy axes towards the direction of the excitation field becomes stronger with increasing H_{ac} .

3.2.3. Distribution of the angle between \vec{n} and \vec{H}

As mentioned in Fig. 3, for the case of sample 2, the angle of the easy axis in the equilibrium state, θ_{ea} , is almost constant and independent of $H(t)$. Following that result, in Fig. 5 the distribution of θ_{ea} for sample 2 is shown when $H_{dc} = 0$ and $\mu_0 H_{ac} = 3$ mT. Here, the vertical axis represents the value of $W_{ea}(\theta_{ea}) \sin \theta_{ea}$, which gives the probability density of MNPs with respect to θ_{ea} . The symbols show the simulation result. The dotted line shows the curve of $W_{ea}(\theta_{ea}) \sin \theta_{ea} = \sin \theta_{ea}$, corresponding to the case when the easy axes are randomly orientated.

As shown by the dotted line, the value of $W_{ea}(\theta_{ea}) \sin \theta_{ea}$ has a peak at $\theta_{ea} = 90^\circ$ when easy axes are randomly orientated. On the other hand, the simulation result shows that the peak is obtained at $\theta_{ea} = 30^\circ$. This is because the easy axes are orientated toward the direction of the excitation field.

As shown above, the easy axes gradually align along the AC field. This is similar to the case when a DC field is applied. Therefore, as in the case of the DC field, we assume that $W_{ea}(\theta_{ea})$ is

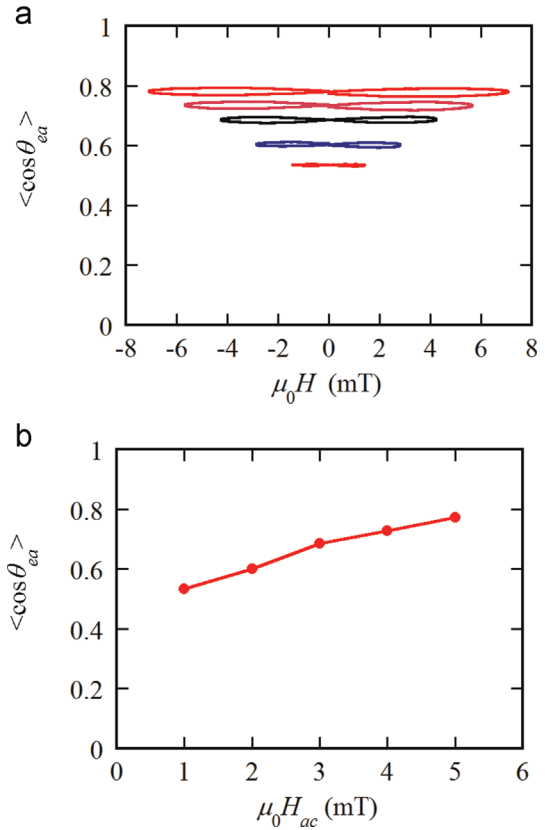


Fig. 4. (a) Traces of the easy axes of sample 2 in an equilibrium state when the values of H_{ac} are changed from $\mu_0 H_{ac} = 1$ –5 mT with $H_{dc} = 0$. (b) Dependence of $\langle \cos \theta_{ea} \rangle$ on H_{ac} .

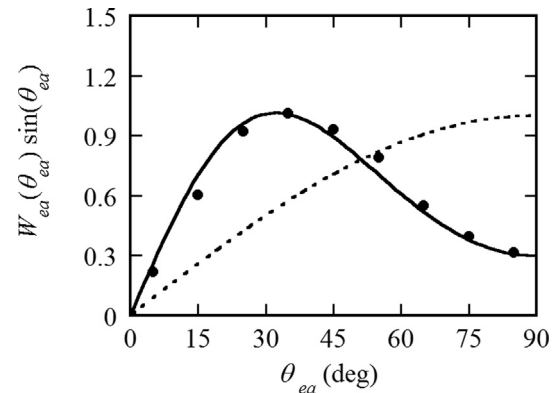


Fig. 5. Probability density of MNPs, $W_{ea}(\theta_{ea}) \sin \theta_{ea}$, as a function of the angle θ_{ea} . Symbols represent simulation result, while solid line represents a distribution of θ_{ea} calculated with Eq. (10) when sample 2 was exposed to an AC field with $\mu_0 H_{ac} = 3$ mT. The dotted line represents the distribution of θ_{ea} for the case when the easy axes are randomly orientated.

given by the Maxwell–Boltzmann distribution [15]

$$W_{ea}(\theta_{ea}) = W_0 [\exp(\xi_{ac} \cos \theta_{ea}) + \exp(-\xi_{ac} \cos \theta_{ea})], \quad (10)$$

where $\xi_{ac} = \mu_0 m H_{ac} / k_B T$. The constant value W_0 is calculated using $\int_0^{\pi/2} W_0 [\exp(\xi_{ac} \cos \theta_{ea}) + \exp(-\xi_{ac} \cos \theta_{ea})] d\theta_{ea} = 1$. Note that the second term on the right is added in Eq. (10) because we define the region of θ_{ea} from 0° to 90° .

The solid line in Fig. 5 shows $W_{ea}(\theta_{ea}) \sin \theta_{ea}$ calculated with Eq. (10). As can be seen, the calculated result agrees well with the simulation depicted by symbols. Therefore, the empirical expression for $W_{ea}(\theta_{ea})$ given in Eq. (10) will be used for the distribution of the easy axes caused by the AC field.

4. Discussion

4.1. M – H curve

We first discuss the effect of the distribution of the angle of the easy axes, $W_{ea}(\theta_{ea})$, on the magnetization. The static M – H curve can be calculated as follows. For the MNPs, whose easy axis is inclined by θ_{ea} with respect to the external field, the static magnetization is given by [15]

$$\frac{M(\theta_{ea})}{M_s} = \frac{\int_{\theta=0}^{\pi} \int_{\phi=0}^{2\pi} \exp(\xi \cos \theta - \sigma \sin^2 \alpha) \sin \theta \cos \theta d\phi d\theta}{\int_{\theta=0}^{\pi} \int_{\phi=0}^{2\pi} \exp(\xi \cos \theta - \sigma \sin^2 \alpha) \sin \theta d\phi d\theta}, \quad (11)$$

where α , given by $\cos \alpha = \sin \theta_{ea} \sin \theta \cos \phi + \cos \theta_{ea} \cos \theta$, is an angle between the easy axis and magnetic moment \vec{m} of an MNP. $\xi = \mu_0 m H / k_B T$ and $\sigma = E_B / k_B T$.

The total magnetization of the sample can be obtained by summing $M(\theta_{ea})$ over all angles. Considering the distribution of the easy axes, W_{ea} , the total magnetization M in the direction of the external field is given by

$$\frac{M}{M_s} = \frac{\int_0^{\pi/2} (M(\theta_{ea}) / M_s) W_{ea}(\theta_{ea}) \sin \theta_{ea} d\theta_{ea}}{\int_0^{\pi/2} W_{ea}(\theta_{ea}) \sin \theta_{ea} d\theta_{ea}}. \quad (12)$$

The static M – H curve calculated from Eqs. (11) and (12) is shown in Fig. 6. The solid line is calculated using the simulation result of $W_{ea}(\theta_{ea}) \sin \theta_{ea}$ depicted by the symbols in Fig. 5. The dash-dotted line represents the result obtained when we assume that the easy axes are randomly orientated, i.e., for the case of $W_{ea}(\theta_{ea}) \sin \theta_{ea} = \sin \theta_{ea}$. The dotted line represents a Langevin function $M/M_s = \cot h(\xi) - 1/\xi$, which can be obtained for the case of $\sigma = 0$.

As can be seen, the M – H curves obtained for the three cases are different. This result indicates that the M – H curve is affected by both the anisotropy energy barrier, σ , and the distribution of the easy axes, $W_{ea}(\theta_{ea})$. As a result, a simple Langevin function cannot explain the M – H curve of the sample 2.

4.2. Harmonic signals

Based on the above discussion, we calculated the third harmonics for both samples. In sample 1, the Brownian process dominates magnetization, which can be represented by the Langevin function. The third harmonic for sample 1 can be calculated with the following equations:

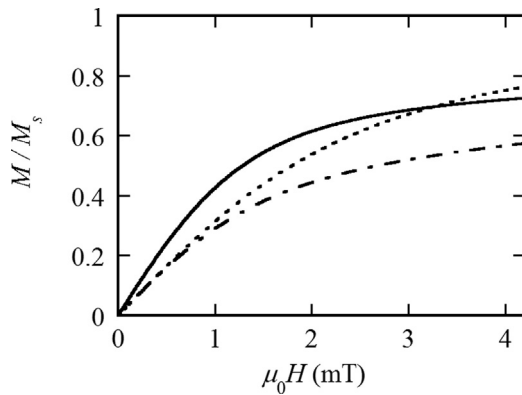


Fig. 6. M – H curves. The solid line is calculated using Eqs. (11) and (12) with the distribution of angle θ_{ea} depicted by the symbols in Fig. 5. The dash-dotted line represents an M – H curve for the case when easy axes are randomly orientated. Dotted line represents a Langevin function.

$$\frac{M_3}{M_s} = \int_0^{1/f} L(\xi(t)) \sin(3 \times 2\pi f t) dt, \quad (13)$$

$$\xi(t) = \frac{\mu_0 m}{k_B T} [H_{dc} + \sqrt{2} H_{ac} \sin(2\pi f t)]. \quad (14)$$

The dotted line in Fig. 2 represents the dependence of third harmonics on H_{dc} when $\mu_0 H_{ac} = 3$ mT. As shown, the result calculated from Eq. (13) agrees well with the simulation results obtained using stochastic equations (Eqs. (1) and (4)).

In sample 2, magnetization is dominated by the Néel process, as mentioned previously. When Néel relaxation time is much less than the inverse of the excitation frequency f , magnetization follows the external field without a phase lag. Therefore, in a manner similar to the static case given in Eqs. (11) and (12), magnetization $M(t)$ is given by

$$\frac{M(t)}{M_s} = \frac{\int_0^{\pi/2} (M(\theta_{ea}, t) / M_s) W_{ea}(\theta_{ea}, \xi_{eff}) \sin \theta_{ea} d\theta_{ea}}{\int_0^{\pi/2} W_{ea}(\theta_{ea}, \xi_{eff}) \sin \theta_{ea} d\theta_{ea}}, \quad (15)$$

with

$$\frac{M(\theta_{ea}, t)}{M_s} = \frac{\int_0^{\pi} \int_0^{2\pi} \exp(\xi(t) \cos \theta - \sigma \sin^2 \alpha) \sin \theta \cos \theta d\phi d\theta}{\int_0^{\pi} \int_0^{2\pi} \exp(\xi(t) \cos \theta - \sigma \sin^2 \alpha) \sin \theta d\phi d\theta}, \quad (16)$$

$$\xi_{eff} = \frac{\mu_0 m \sqrt{H_{dc}^2 + H_{ac}^2}}{k_B T}. \quad (17)$$

We tentatively assume that the distribution of the easy axes, $W_{ea}(\theta_{ea})$, is determined by the parameter ξ_{eff} given in Eq. (17) when both AC and DC fields are applied. Then, by performing the Fourier transform, the third harmonics for sample 2 can be calculated as

$$M_3/M_s = \int_0^{1/f} M(t)/M_s \sin(3 \times 2\pi f t) dt. \quad (18)$$

The solid line in Fig. 2 represents the dependence of third harmonics on H_{dc} calculated using Eqs. (15)–(18) when $\mu_0 H_{ac} = 3$ mT. As shown, the calculated result agrees reasonably well with the simulation results of stochastic Eqs. (1) and (4).

Finally, we comment on the value of M_3 between simulation and measurement. As shown in Figs. 1 and 2, relative height of M_3 for sample 1 and sample 2 was reversed between experimental and simulated results. This reversal will be caused by the distribution of the particle size in the sample, which was not taken into account in the present simulation. When the size distribution exists, only a certain portion of MNPs in the sample can respond to the AC excitation field. It is well recognized that the portion becomes larger in the case of Brownian relaxation, compared to the case of Néel relaxation. This is because the dependence of the Néel relaxation time on the particle size is much stronger than the case of Brownian relaxation. In sample 1, MNPs were diluted with pure water, and their behavior was dominated by Brownian relaxation. On the other hand, MNPs were diluted with glycerol in sample 2, and their behavior was dominated by Néel relaxation. Therefore, we can expect that the signal from the sample 1 becomes larger than that of sample 2, as shown in the experimental result (Fig. 1).

5. Conclusions

We explored the effect of viscosity on harmonic signals from a magnetic fluid. First, we showed that the measured dependence of the third harmonic signal on the DC external field is different

between magnetic fluids diluted with glycerol and pure water. To understand the mechanism that causes this difference, we performed a numerical simulation based on the stochastic LLG and Langevin equations, in which both the Brownian and Néel relaxations are taken into account. Using the simulation results, we clarified how the magnetization mechanism is affected by the viscosity of the fluid. For the case of $\tau_B \ll 1/2\pi f$, magnetization can be described by the Langevin function. On the other hand, for the case of $\tau_N \ll 1/2\pi f \ll \tau_B$, the easy axes of the MNPs turn toward the direction of the external field in an equilibrium state. Consequently, the magnetization in a high-viscosity medium is different from the Langevin function even though the Néel relaxation time is less than the time period of the external field. The alignment of easy axes of the MNPs caused by an AC field can be empirically expressed with Eq. (10).

Acknowledgments

This work was partly supported by the Japan Society for the Promotion of Science KAKENHI Grant numbers 24246072 and 26820159.

References

- [1] Q.A. Pankhurst, N.T.K. Thanh, S.K. Jones, J. Dobson, Progress in applications of magnetic nanoparticles in biomedicine, *J. Phys. D: Appl. Phys.* **42** (2009) 224001.
- [2] B. Gleich, J. Weizenecker, Tomographic imaging using the nonlinear response of magnetic particles, *Nature* **435** (2005) 1214–1217.
- [3] T. Knopp, S. Biederer, T. Sattel, J. Weizenecker, B. Gleich, J. Borgert, T.M. Buzug, Three-dimensional real-time in vivo magnetic particle imaging, *Phys. Med. Biol.* **54** (2009) L1–L10.
- [4] T. Knopp, T.F. Sattel, S. Biederer, J. Rahmer, J. Weizenecker, B. Gleich, J. Borgert, T.M. Buzug, Model-based reconstruction for magnetic particle imaging, *IEEE Trans. Med. Imaging* **29** (2010) 12–18.
- [5] P.W. Goodwill, G.C. Scott, P.P. Stang, S.M. Conolly, Narrowband magnetic particle imaging, *IEEE Trans. Med. Imaging* **28** (2009) 1231–1237.
- [6] P.W. Goodwill, S.M. Conolly, The X-space formulation of the magnetic particle imaging process: 1-D signal, resolution, bandwidth, SNR, SAR, and magnetostimulation, *IEEE Trans. Med. Imaging* **29** (2010) 1851–1859.
- [7] P.W. Goodwill, E.U. Saritas, L.R. Croft, T.N. Kim, K.M. Krishnan, D.V. Schaffer, S.M. Conolly, X-space MPI: magnetic nanoparticles for safe medical imaging, *Adv. Mater.* **24** (2012) 3870–3877.
- [8] S. Biederer, T. Knopp, T.F. Sattel, K. Lüdtke-Buzug, B. Gleich, J. Weizenecker, J. Borgert, T.M. Buzug, Magnetization response spectroscopy of superparamagnetic nanoparticles for magnetic particle imaging, *J. Phys. D: Appl. Phys.* **42** (2009) 205007.
- [9] R.M. Ferguson, K.R. Minard, K.M. Krishnan, Optimization of nanoparticle core size for magnetic particle imaging, *J. Magn. Magn. Mater.* **321** (2009) 1548–1551.
- [10] R.M. Ferguson, K.R. Minard, A.P. Khandhar, K.M. Krishnan, Optimizing magnetite nanoparticles for mass sensitivity in magnetic particle imaging, *Med. Phys.* **38** (2011) 1619–1626.
- [11] T. Yoshida, N.B. Othman, K. Enpuku, Characterization of magnetically fractionated magnetic nanoparticles for magnetic particle imaging, *J. Appl. Phys.* **114** (2013) 173908.
- [12] T. Yoshida, N.B. Othman, T. Tsubaki, J. Takamiya, K. Enpuku, Evaluation of harmonic signals for the detection of magnetic nanoparticles, *IEEE Trans. Magn.* **48** (2012) 3788–3791.
- [13] W.T. Coffey, Y.P. Kalmykov, J.T. Waldron, *The Langevin Equation*, World Scientific, Singapore (1996) 95.
- [14] H. Mamiya, B. Jeyadevan, Hyperthermic effects of dissipative structures of magnetic nanoparticles in large alternating magnetic fields, *Sci. Rep.* **1** (2011) 157.
- [15] W.T. Coffey, P.J. Cregg, Y.P. Kalmykov, in: I. Prigogine, S.A. Rice (Eds.), *Advances in Chemical Physics*, vol. 83, Wiley, New York, 1993, p. 263.